

Field line reconstruction with magneto-acoustic cut-off frequency above sunspots

Ding Yuan¹, R. Sych², V. E. Reznikova³, and V. M. Nakariakov^{1,4}

¹ Centre for Fusion, Space and Astrophysics, Department of Physics, University of Warwick, Coventry CV4 7AL, UK
e-mail: Ding.Yuan@warwick.ac.uk

² Institute of Solar-Terrestrial Physics, Russian Academy of Science, Siberian Branch, 126a Lermontov st., Irkutsk 664033, Russia

³ Center for Mathematical Plasma Astrophysics, Department of Mathematics, KU Leuven, Celestijnenlaan 200B box 2400 BE-3001 Leuven, Belgium

⁴ Central Astronomical Observatory at Pulkovo of the Russian Academy of Sciences, 196140 St Petersburg, Russia

November 26, 2012

ABSTRACT

Context. The cut-off frequency of magneto-acoustic gravity (MAG) waves is known to be lowered by the inclined magnetic field. This effect allows low-frequency waves to penetrate into the upper atmosphere and the corona.

Aims. We estimate the modification of the cut-off frequency at various heights and reconstruct the inclination of the magnetic field according to the magnetoacoustic-gravity wave theory in a stratified solar atmosphere permeated by a uniform magnetic field.

Methods. We used the Pixelised Wavelet Filtering (PWF) method to compute narrow-band power maps of SDO/AIA imaging datasets in the 1700 Å, 1600 Å and 304 Å bandpasses that correspond to different heights. The cut-off frequency was defined as contours where the spectral power dropped to the median level. It was measured as a function of the spatial location. We inferred the magnetic field inclination according to the MAG wave theory in the low- β limit and compared it with the potential field extrapolation.

Results. We analysed intensity oscillations in a symmetric sunspot AR11131 (08 Dec 2010) and an asymmetric sunspot AR11330 (27 Oct 2011). We reconstructed the magnetic field inclination in the radial direction for the symmetric sunspot and in both radial and azimuthal directions for the asymmetric sunspot.

Conclusions. We observed 3D variation of the main oscillation periods in sunspots. We found that shorter-period oscillations were mostly constrained in sunspot umbrae, while longer-period oscillations formed an annular shape enclosing the umbra. Longer periods are found to be distributed further away from the sunspot centre. Our results indicate that 3-min oscillation are generated in the chromosphere, possibly by the acoustic resonator model, while 5-min and longer-period oscillations seemed to originate in a level under the photosphere. The reconstructed field inclinations gives the values of the field inclination that are systematically larger than the values obtained by the potential field extrapolation. The inclined magnetic field line can account for 60-80% of cut-off frequency lowering only.

Key words. Sun: atmosphere - Sun: UV radiation - Sun: oscillations - Sun: sunspots -Sun: magnetic topology

1. Introduction

Magnetoacoustic gravity (MAG) waves in the solar atmosphere are subject to strong dispersion: their properties depend strongly on their frequency. In particular, the parameters of the solar atmosphere determine the MAG cut-off frequency. MAG waves with frequencies below the cut-off value become evanescent, and therefore cannot reach the upper layers of the solar atmosphere. The cut-off value also determines the oscillating frequency of MAG waves as the response of the atmosphere to a broadband (e.g. impulsive) excitation (e.g. Suematsu et al. 1982; Botha et al. 2011). The cut-off frequency for MAG waves was derived for a stratified isothermal solar atmosphere permeated by a uniform magnetic field (Bel & Leroy 1977; Zhugzhda & Dzhililov 1984). It generally depends on the local plasma β ($\beta = 2\mu_0 p/B^2 = 2c_s^2/\gamma V_A^2$, where p is the gas pressure, μ_0 is the magnetic permeability in vacuum space, B is the magnetic field strength, V_A is the local Alfvén speed, c_s is the local sound speed, and $\gamma = 5/3$ is the adiabatic index) and the magnetic field inclination ϕ . In the high- β regions ($\beta \gg 1$, e.g. the photosphere and chromosphere of the quiet Sun), it is reduced into the pure acoustic cut-off frequency

$\nu_0 = \gamma g/4\pi c_s = 5.2$ mHz (with the corresponding cut-off period $p_0 = 3.2$ min), where $g = 274$ m/s is the gravitational acceleration, and $c_s = 7$ km/s is the sound speed estimated for typical chromospheric conditions. In the low- β approximation ($\beta \ll 1$, e.g. in a sunspot or coronal active region), the cut-off frequency is modified by the magnetic inclination $\nu_{ac} = \nu_0 \cos \phi$ (Bel & Leroy 1977)¹. This helps explaining the existence of low-frequency waves in the corona, which are believed to carry a larger portion of energy flux than its high-frequency counterpart (e.g. Fontenla et al. 1993; Jefferies et al. 2006). Also, the study of the effect of the cut-off frequency on compressive waves observed in the solar atmosphere provides us with a seismological tool for the determination of the local geometry of the magnetic field.

According to Bel & Leroy (1977), the low-frequency (long-period) waves are able to penetrate the upper solar atmosphere, along the magnetic concentrations, e.g. sunspots, pores, which work as MAG waveguides. It was suggested that, due to the

¹ The derivations in Bel & Leroy (1977) contain obvious misprints, a follow-up theoretical study will redo the derivation. However the numerical results and figures are reliable. In this work, we use the trustworthy extreme case of $\beta \ll 1$

effect of the magnetic inclination, the 5-min oscillations appear in the chromospheric spicules (De Pontieu et al. 2004) and in coronal loops at active regions (De Moortel et al. 2002; De Pontieu et al. 2005). de Wijn et al. (2009) observed the propagation of solar global p -modes to the chromosphere through the inclined magnetic fields at the periphery of plage regions. Other observations of long-period oscillations in the corona could be attributed to channelling by the inclined field as well (see e.g. Wang et al. 2009; Marsh et al. 2009; Yuan et al. 2011).

A direct observation of the magnetoacoustic cut-off in a sunspot has been performed with full Stokes (I, U, V, Q) spectropolarimetry (see Fig. 5 in Bloomfield et al. 2007). The authors found that the cut-off frequency closely followed the magnetic field modification in the strong-field limit ($\beta \ll 1$) of Bel & Leroy (1977). However no further examination was done to compare the information with the magnetic inclination inverted by full Stokes observables. It appeared that the correlation and phase difference of the time series of the intensity variation obtained at various heights of the solar atmosphere looked more realistic when the offsets at the spatial location were corrected by considering the magnetic inclination (Bloomfield et al. 2007). McIntosh & Jefferies (2006) studied the travel time of narrow-band signals around a sunspot and found good consistency with the prediction of Bel & Leroy (1977) for both the quiet sun ($\beta \gg 1$) and a sunspot ($\beta \lesssim 1$). Tziotziou et al. (2006) applied the empirical formula $\nu_{\text{peak}}(\phi) \approx 1.25\nu_{\text{ac}}(\phi)$, where ν_{peak} denotes the peak frequency at each location, ν_{ac} indicates the corresponding magnetoacoustic cut-off frequency, to the waves observed in a sunspot's chromosphere, and estimated the magnetic field inclination $\phi = \arccos[\nu_{\text{peak}}/(1.25 \times \nu_0)]$ (Bogdan & Judge 2006). Reznikova et al. (2012) compared the spectra and phase relations of the UV and EUV emission intensity at various heights of the solar atmosphere to identify the features of upwardly propagating waves and found that the variation of the cut-off frequency across the umbra was consistent with Bel & Leroy (1977). The follow-up study (Reznikova & Shibasaki 2012) compared the observational MAG cut-off frequencies in AIA 304 Å with the values obtained by the potential field extrapolation (Sakurai 1982) and found good agreement.

In Bel & Leroy (1977), an adiabatic plasma was implicitly assumed, while in the photosphere and chromosphere, radiative loss is of significance. Centeno et al. (2006, 2009) used a linear wave equation with a radiative cooling term and explained well the observed phase delay and wave amplitude variation with height in both sunspots and pores. A detailed study using multiple spectral lines formed at different heights was presented in Felipe et al. (2010). The connectivity of different layers of the atmosphere determined by the phase difference and power amplification was demonstrated. Therefore, the study of the cut-off frequency can also retrieve the plasma parameters associated with radiative loss.

The cut-off frequency detected in a sunspot atmosphere is a good indicator of local plasma parameters, therefore it can be used to diagnose the local atmosphere, e.g. temperature, magnetic inclination. In our study, we present the observation of the spatial distribution and height variation of the cut-off frequency with SDO/AIA (Lemen et al. 2011; Boerner et al. 2011) and inferred the magnetic field inclination. The observational results were used for the reconstruction of the 3D geometry of the magnetic field. The information was deployed to diagnose the magnetic field inclination. In this paper, we present the analysed data sets in Sec. 2. The methods are summarised in Sec. 3. Then we compare the diagnostic results with the potential field extrapolation in Sec. 4, and conclusions are given in Sec. 5.

2. Observations

We selected two large sunspots associated with well-developed active regions in the corona, where outwardly propagating EUV disturbances were persistently detectable. We chose good observation intervals without disruptions from either flares or other transient events. The observation intervals correspond to the days when the sunspots were crossing the central meridian: they were least affected by Wilson depression (Loughhead & Bray 1958) and were well exposed for imaging.

The first sunspot was associated with AR11131 situated near the 30° latitude in the northern hemisphere. It crossed the central meridian on 08 Dec 2010. It consisted of a strong magnetic concentration of the south polarity, while the north polarities were spread sparsely to the west and north of the central sunspot, therefore the sunspot had a pretty symmetric shape without any trailing sunspot, see Fig. 1 (top). We used AIA data sets of 1600 Å, 1700 Å and 304 Å from 02:30 to 03:30 UT on 08 Dec 2010. The cadence time was 24 s for 1600 Å and 1700 Å images, and 12 s for 304 Å images. This sunspot was also analysed in Reznikova et al. (2012); Reznikova & Shibasaki (2012).

The second sunspot chosen for this study was the leading main sunspot on the eastern part of active region AR11330 situated slightly to the north of the solar equator. The trailing sunspot group of north polarity was about 150 Mm to the main sunspot. It formed into a non-symmetric shape with a protrusion due to the tearing of the other polarity (see B_{LOS} in Fig. 1 (e)). The shape was inherited at the temperature minimum (1700 Å, see Fig. 1 (f)), the photosphere and transition region (1600 Å, see Fig. 1 (g)). In the chromosphere (304 Å, Fig. 1 (h)), the shape was less pronounced and was replaced by a far-extending fan structure. The study of propagating EUV disturbances in the coronal fan over this sunspot was presented in Yuan & Nakariakov (2012). We used one-hour data sets from 04:00 to 05:00 UT on 27 Oct 2011 in 1700 Å, 1600 Å and 304 Å. The instrumentation and data preparation are presented in Yuan & Nakariakov (2012). The cadence time was 24 s and 12 s for EU and EUV images, respectively.

3. Methods

3.1. Power map by Pixelised Wavelet Filtering

The Pixelised Wavelet Filtering (PWF) method was developed by Sych & Nakariakov (2008). It is based on the wavelet transform and is well validated in determining the spatial, temporal and phase structure of oscillations in an imaging cube $I_\lambda(x, y, t)$, where λ is the wavelength of the data channel, x, y and t are the discrete spatial locations and the measuring times, respectively. It gives the spatial distribution of the amplitude (power), frequency and phase of a signal in the spectral interval of interest.

For data sets $I_\lambda(x, y, t)$, we performed PWF analysis and obtained narrow-band power maps $P_\nu^\lambda(x, y)$ (or $P_p^\lambda(x, y)$, where $p = \nu^{-1} = 2, \dots, 20$ min with the resolution of $dp = 0.1$ min). In a sunspot, the power distribution normally forms a filled disk (short periods / high frequencies) or a power ring (long period / low frequencies) concentric at the sunspot centre (e.g. Sych & Nakariakov 2008; Reznikova et al. 2012). Therefore, to facilitate quantitative analysis, the power maps were transformed into a polar coordinate system with the origin coinciding with the sunspot centre $P_\nu^\lambda(r, \theta)$, where r is the distance to the sunspot centre, θ is the polar angle relative to the horizontal line pointing to the solar west (see Fig. 1 (a) and (e)).

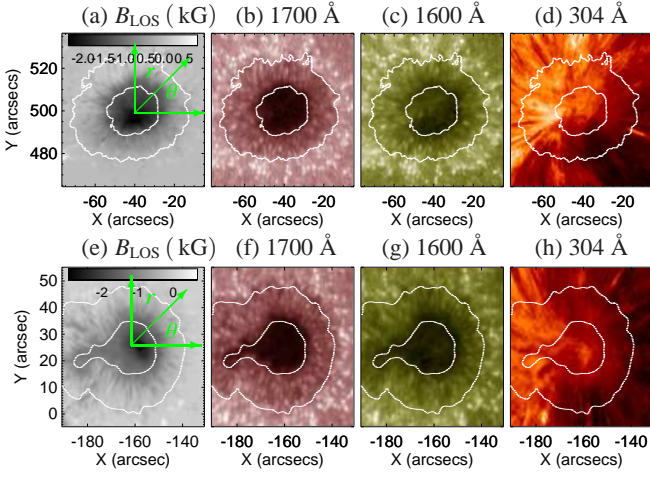


Fig. 1. Multi-instrumental imaging of AR11131 (top, 08 Dec 2010) and AR11330 (bottom, 27 Oct 2011) and the underlying sunspots at different heights. (a) and (e): The LOS magnetic field strength determined with HMI. The polar coordinate systems used in this study are overlaid. (b) - (d) and (f) - (h): AIA intensity images on logarithmic scales at different observational wavelengths show different levels of the sunspots and the associated active regions. In order of increasing heights of the observed levels, the displayed images illustrate the temperature minimum level (1700 Å), upper photosphere and transition region (1600 Å), and the chromosphere (304 Å). The dotted lines show the border of the sunspot umbra and penumbra determined with the 4500 Å image.

For the power maps $P_v(r, \theta)$, the denotation λ is dropped to refer to the general case that is applicable to all wavelengths. We computed the maximum power at each location $P_{\max}(r, \theta)$ (see panel (a) in Fig. 3, Fig. 4 and Fig. 5). The corresponding peak period is $p_{\text{peak}}(r, \theta)$ (see panel (b) in Fig. 3, Fig. 4 and Fig. 5). The dependence of $p_{\text{peak}}(r, \theta)$ shows the spatial distribution of the period with the dominant oscillating power, while $P_{\max}(r, \theta)$ illustrates the significance of these oscillations. The variance of the spectral power over the spectrum for each pixel was also calculated, $\text{Var}(r, \theta) = \text{Var}(P_v(r, \theta))_v^2$ (see Fig. 3 (d)). This value is a good indicator of the significance of the signal at a specific location. To estimate the 1σ noise level, we took the average over the spectrum $\sigma(r, \theta) = \langle P_v(r, \theta) \rangle_v$ (see example in Fig. 3(e)). For the analysis of the symmetric sunspot, a further averaging over the polar angle θ was performed to reduce the θ dimension. Table 1 summarises the denotations and their physical meanings in both 1D and 2D cases.

Several typical narrow-band power maps obtained in 304 Å bandpass on 08 Dec 2010 are shown in Fig. 2 (also see Fig. 7 of Reznikova et al. 2012). For the periods less than 3.2 min (frequencies greater than 5.2 mHz), the dominant power fills up the umbral region. The inhomogeneity of the power distribution implies a fine structure in the umbra (see the study in Jess et al. 2012, using imaging data with a resolution of 50 km/pixel in contrast to 430 km/pixel of AIA images). For the periods greater than 3.2 min, the power of significant oscillations is normally concentrated in an annular structure enclosing the umbra. The annulus expands with the increasing

² The subscript v means the operation(s) along the spectral dimension. With the same philosophy, the subscripts θ and r mean the operation(s) along the polar angle dimension and radial distance dimension, respectively.

period. We interpret this phenomenon as modification of the cut-off frequency by the inclined magnetic field (Bel & Leroy 1977; De Pontieu et al. 2004, 2005; McIntosh & Jefferies 2006, see discussions in Reznikova et al. (2012)). As the magnetic field lines approach the outer penumbra, the inclination angle becomes larger, therefore the cut-off frequency is lowered to a smaller value (Bel & Leroy 1977), and allows the channelling of upwardly propagating waves of lower frequency (longer period).

3.2. 1D reconstruction in symmetric sunspot (08 Dec 2010)

3.2.1. Reconstruction of field line inclination by MAG cut-off

For the symmetric sunspot observed AR11131 (08 Dec 2010), we present the example of 304 Å data in Fig. 3. The distribution of the peak power $P_{\max}(r, \theta)$ and the corresponding peak period $p_{\text{peak}}(r, \theta)$ are illustrated in Fig. 3 (a) and Fig. 3 (b), respectively. The dominant oscillating power fills in the umbra and gradually decreases further out in the penumbra and arcade region. In the umbra, the peak period is the well-known chromospheric 3-min oscillation (see review paper Bogdan & Judge 2006). It fills up the whole umbra and a tiny part of the penumbra. In the penumbra, the peak period gradually increases with the radial distance from sunspot centre, indicating the modification of the cut-off frequency by inclined magnetic field lines. The variation with the polar angle is found to be very small. We averaged the power along the polar angles and obtained the normalised power $P_v(r)$ as a function of the distance to the sunspot centre, r , and the frequency ν , as shown in Fig. 3 (c). We defined the contour of the global median in $P_v(r)$ as the curve of the cut-off period $p_{\text{ac}}(r)$ (or frequency $\nu_{\text{ac}}(r) = 1/p_{\text{ac}}(r)$, see Fig. 3 (c)).

According to Bel & Leroy (1977), the MAG cut-off frequency in the low- β approximation is modified when the magnetic field line is inclined from the vertical direction, $\nu_{\text{ac}} = \nu_0 \cos \phi$. We estimated the inclination angle ϕ by

$$\phi(r) = \arccos \frac{\nu_{\text{ac}}(r)}{\nu_0} = \arccos \frac{p_0}{p_{\text{ac}}(r)} \quad (1)$$

where $\nu_0 = 5.2$ mHz ($p_0 = 3.2$ min) is the acoustic cut-off frequency (period) (see Fig. 3 (f)).

3.2.2. Error and significance analysis

According to (1), the uncertainty of ϕ is calculated as

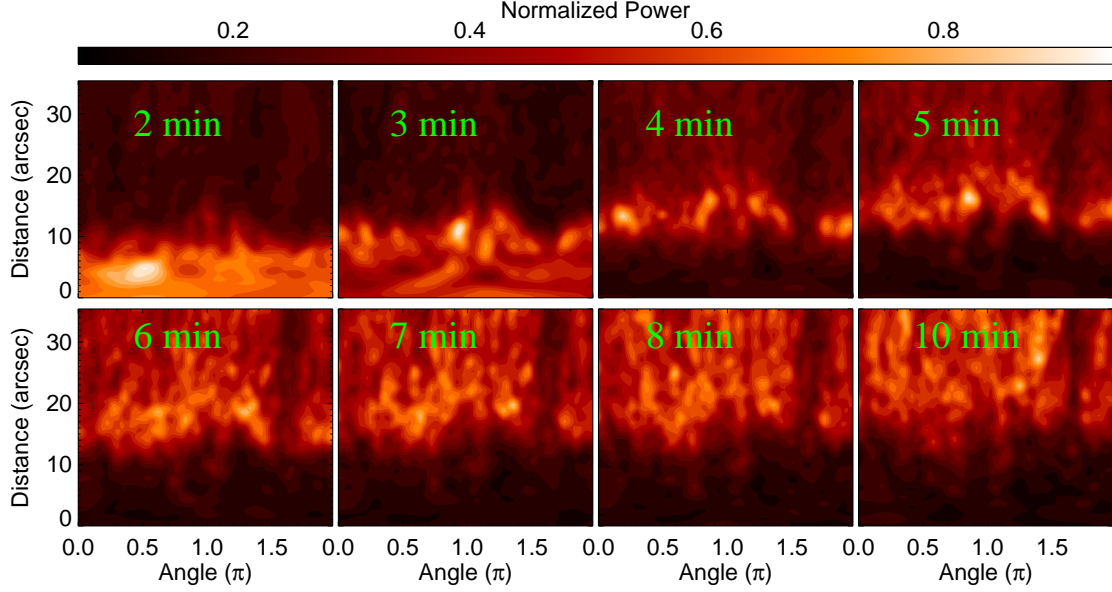
$$\Delta\phi(r) = \frac{\Delta\nu_{\text{ac}}(r)}{\sqrt{\nu_0^2 - \nu_{\text{ac}}^2(r)}} = \frac{\cos^2 \phi}{\sqrt{1 - \cos^2 \phi}} \frac{\Delta p_{\text{ac}}(r)}{p_0} \quad (2)$$

which requires the estimation of Δp_{ac} . This quantity can be assumed to be proportional to the noise level $\sigma(r)$, and the spread (standard deviation) of the spectral power over the polar angle $s(r)$. Δp_{ac} should also be inversely proportional to the maximum spectral power $P_{\max}(r)$ and the square root of the number of the data point in polar angles, $\sqrt{N_\theta}$. The noise level $\sigma(r)$ is found to vary between 0.16 and 0.36. When we normalise it with its total median, it gives a factor between 0.52 and 1.13 to the uncertainty. We did the same to the spread $s(r)$ and obtained another factor between 0.31 and 1.4 added to the error bar. The value of $P_{\max}(r)$ changes from 1 to about 0.4 with r , giving a factor from about 1 to about 2.5 to the total error bar. We choose a constant $dp = 0.1$ min, the spectral resolution of PWF analysis, therefore the total uncertainty becomes

$$\Delta p_{\text{ac}}(r) = \frac{\sigma(r)}{\text{Med}(\sigma(r))} \frac{s(r)}{\text{Med}(s(r))} \frac{dp}{\sqrt{N_\theta} P_{\max}(r)}. \quad (3)$$

Table 1. Notations used in the paper.

Physical meaning	2D denotation	Physical meaning	1D denotation
2D spectral power map	$P_v(r, \theta)$	1D spectral power map	$P_v(r) = \langle P_v(r, \theta) \rangle_\theta$
2D spectral noise level	$\sigma(r, \theta) = \langle P_v(r, \theta) \rangle_v$	1D spectral noise level	$\sigma(r) = \langle P_v(r) \rangle_v$
2D spectral power variance	$\text{Var}(r, \theta) = \text{Var}(P_v(r, \theta))_v$	1D spectral power variance	$\text{Var}(r) = \text{Var}(P_v(r))_v$
2D spectral peak power	$P_{\max}(r, \theta) = \max(P_v(r, \theta))_v$	1D spectral peak power	$P_{\max}(r) = \max(P_v(r))_v$
2D peak period	$p_{\text{peak}}(r, \theta)$	1D peak period	$p_{\text{peak}}(r)$ for all θ
2D MAG cut-off period	$p_{\text{ac}}(r, \theta)$	1D MAG cut-off period	$p_{\text{ac}}(r)$ for all θ
2D MAG cut-off frequency	$\nu_{\text{ac}}(r, \theta) = 1/p_{\text{ac}}(r, \theta)$	1D MAG cut-off frequency	$\nu_{\text{ac}}(r) = 1/p_{\text{ac}}(r)$
...	...	1D power spread	$s(r) = \text{stdev}(P_v(r, \theta))_\theta _{v=\nu_{\text{ac}}}$

**Fig. 2.** Typical narrow band power maps of 304 Å bandpass in polar coordinate made for 08 Dec 2010.

When the cut-off period approaches the detection limit (20 min in our application), the observation of the cut-off effect becomes less reliable. Applying this limit, we estimated the regions of significant measurements. We estimated the noise in the spectra as $\sigma(r, \theta) = \langle P_v(r, \theta) \rangle_v$. The noise level is illustrated in Fig. 3 (e). It was further averaged over the polar angles, $\sigma(r) = \langle P_v(r, \theta) \rangle_{\theta, v}$. The measurements with the noise level distributed above 68% (more than a standard deviation above the mean) of the noise are considered as less reliable (see the cross-hatched regions in all panels of Fig. 3). An alternative way is to consider the variance of the power maps, which reflects the contrast of the oscillating powers, giving us the significance of the measurements. We excluded 23% (lower than one standard deviation below the mean) of the smaller portion of the power variance distribution. As the results determined with the use of either power variance or noise distribution are almost similar, we utilised only the results quantified by the noise level in the significance analysis.

3.3. 2D reconstruction in asymmetric sunspot (27 Oct 2011)

In 2D spectral power maps, we consider the areas with the spectral power above the median of the corresponding narrow-band power map as regions that allowed upward propagating MAG waves. The borders of these areas were defined as contours of the MAG cut-off. By labelling the cut-off contours, we were able to reconstruct the field line inclination.

The reconstruction steps are similar to those in the 1D case. The estimation of the error, $\Delta p_{\text{ac}}(r, \theta)$, is simplified,

$$\Delta p_{\text{ac}}(r, \theta) = \frac{\sigma(r, \theta)}{\text{Med}(\sigma(r, \theta))} \frac{dp}{P_v(r, \theta)} \quad (4)$$

We masked out the regions with the less significant measurements. The masks were designed with two criteria: 1) the pixel should be within the penumbra and umbra; 2) the noise level in that pixel should not exceed the 68% level in $\sigma(r, \theta)$ distribution. Only the measurements within the mask are shown in Fig. 6, Fig. 7 and Fig. 8

3.4. Magnetic field extrapolation

We compare the field reconstruction with 3D magnetic field extrapolation. Potential (current-free) fields were extrapolated using the MAGPACK2 package (Sakurai 1982). The current-free model in this code is based on the Green's function method and requires a line-of-sight magnetogram as the bottom boundary condition. Although, we can not *a priori* exclude the presence of the electric currents in the considered volume, we have chosen this model because of the following reasons: 1) both of ARs did not produce any flares within or close to our observational intervals; 2) we are interested in field structures in the layers below the corona where the dense material can influence the field inclination. Therefore, the choice of the non-potential field is unlikely to produce better approximation at these heights.

Fig. 9 presents a 2D projection of reconstructed magnetic field lines overlaid on the photospheric line-of-sight magnetogram (a) sunspot AR11131 (08 Dec 2010) and (b) sunspot

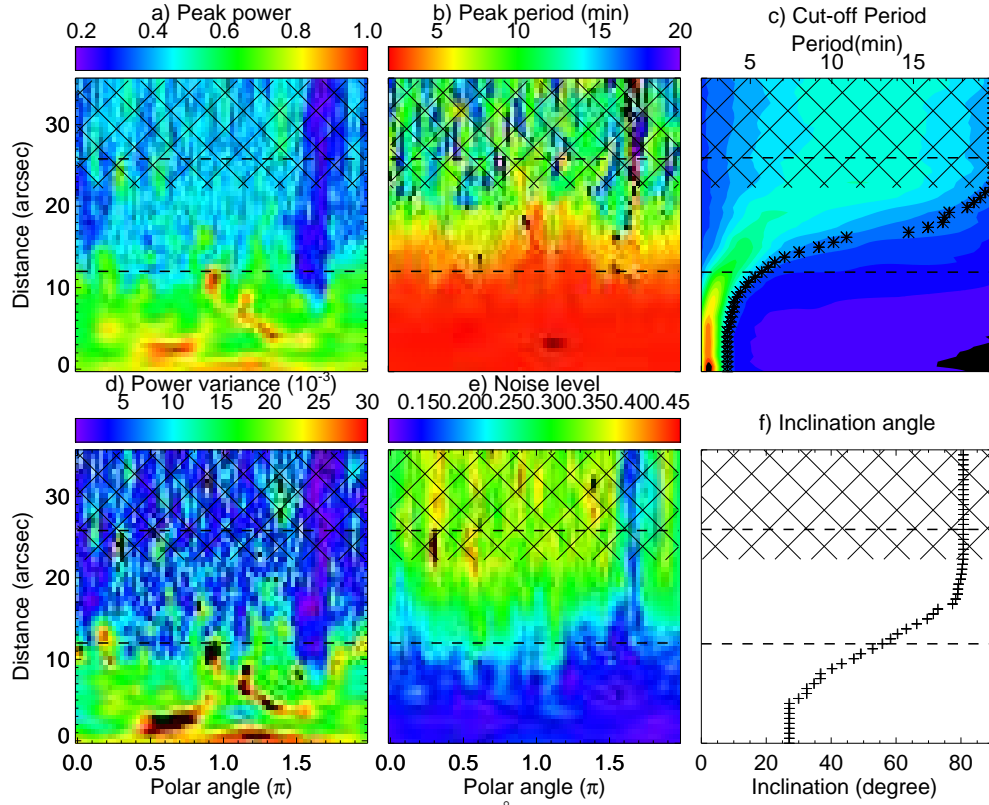


Fig. 3. The oscillating power information extracted from the 304 Å data set of the sunspot AR11131 (08 Dec 2010), shown in the polar coordinates (r and θ). The dashed lines mark the borders of the umbra and penumbra. The unreliable region is cross-hatched. a) The peak power distribution. b) The peak period distribution. c) The 1D spectral power map as a function of r and p . The contour in asterisk shows the cut-off period. d) The spectral power variance distribution. e) The spectral noise distribution. f) The reconstruction of the magnetic field inclination.

1 AR11330 (27 Oct 2011). The colour coding represents the mag-
 2 netic field strength, using blue for southern (negative) and red
 3 for northern (positive) polarities. For the sunspot AR11131, we
 4 selected sub-area of $160'' \times 160''$ from the SOHO/MDI full-disk
 5 magnetogram taken at 04:51 UT, as shown in Fig. 9(a). For the
 6 sunspot AR11330, the HMI line-of-sight magnetogram was ob-
 7 tained as a level-1.5 FITS file. A larger size of $300'' \times 300''$ was
 8 selected to include the sufficient amount of positive polarity fol-
 9 lowing the main sunspot. The magnetic field was computed with
 10 a $2''$ mesh spacing using a spherical boundary.

11 4. Results

12 4.1. Spatial and height distribution of dominant oscillations

13 Based on the 1D power distribution, panel (c) of Fig. 3, Fig. 4
 14 and Fig. 5, it is clearly seen that 3-min oscillations are very
 15 strictly constrained within the umbra region, while 5-min oscil-
 16 lations dominate only at a thin annulus (about 2.9 - 5.0 Mm in
 17 width) between the umbra and penumbra. Although 3-min oscil-
 18 lation is strongest in the umbra, it is predominant within the disks
 19 of radii about 2.1, 5.8 and 7.2 Mm in the 1700 Å (temperature
 20 minimum), 1600 Å (upper photosphere) and 304 Å (chromo-
 21 sphere) data, respectively. Although 3-min oscillation can prop-
 22 agate through both vertical and inclined magnetic field, it is con-
 23 strained only in the umbra. This implies that the 3-min oscilla-
 24 tion is not likely to originate from the solar interior. Instead, it
 25 is consistent with the acoustic resonator model (Zhugzhda 2008;
 26 Botha et al. 2011). The 5-min oscillation is well pronounced in
 27 the 1700 Å data. It appears that there is strong interaction be-

tween the magnetic fields and the ambient plasma enclosing the
 sunspot umbra, where the magnetic field is medium in strength
 and slightly inclined and has a strong longitudinal gradient. It
 seems there is strong p -mode absorption at the umbra border.
 The maximum energy transmission was predicted to occur at the
 height where the Alfvén speed is equivalent to the local sound
 speed and at an attack angle of about 30° (Cally et al. 2003;
 Schunker & Cally 2006). Thus the 5-min oscillation may form
 at the temperature minimum (about 500 km above the photo-
 sphere). The 2D power maps also confirm these results, see pan-
 els a) and b) in Fig. 3, Fig. 4, Fig. 5, Fig. 6, Fig. 7 and Fig. 8.
 In panel (a) of Fig. 3 and Fig. 6, the power of 3-min oscillations
 show variations within the umbra. This implies fine structuring
 inside the umbra. Stronger sources of oscillations were found
 better correlated with the 3-min propagating disturbances in the
 corona loops in 171 Å bandpass (Jess et al. 2012; Sych et al.
 2012). A dedicated phase study of the oscillations at various
 heights of the sunspot atmosphere will be presented in a follow-
 up paper.

47 4.2. Correlation of the peak and cut-off frequencies

The detected cut-off frequencies are plotted versus the corre-
 sponding peak frequencies, see Fig. 10. The correlation between
 them is very high: the Pearson's correlation coefficients R are
 0.98, 0.94 and 0.99 for the 1700 Å, 1600 Å and 304 Å data,
 respectively. We fitted a linear relationship ($v_{ac} = av_{peak} + b$)
 to the data using the MPFITEXY routine³ (Williams et al.

³ <http://purl.org/mike/mpfitexy>

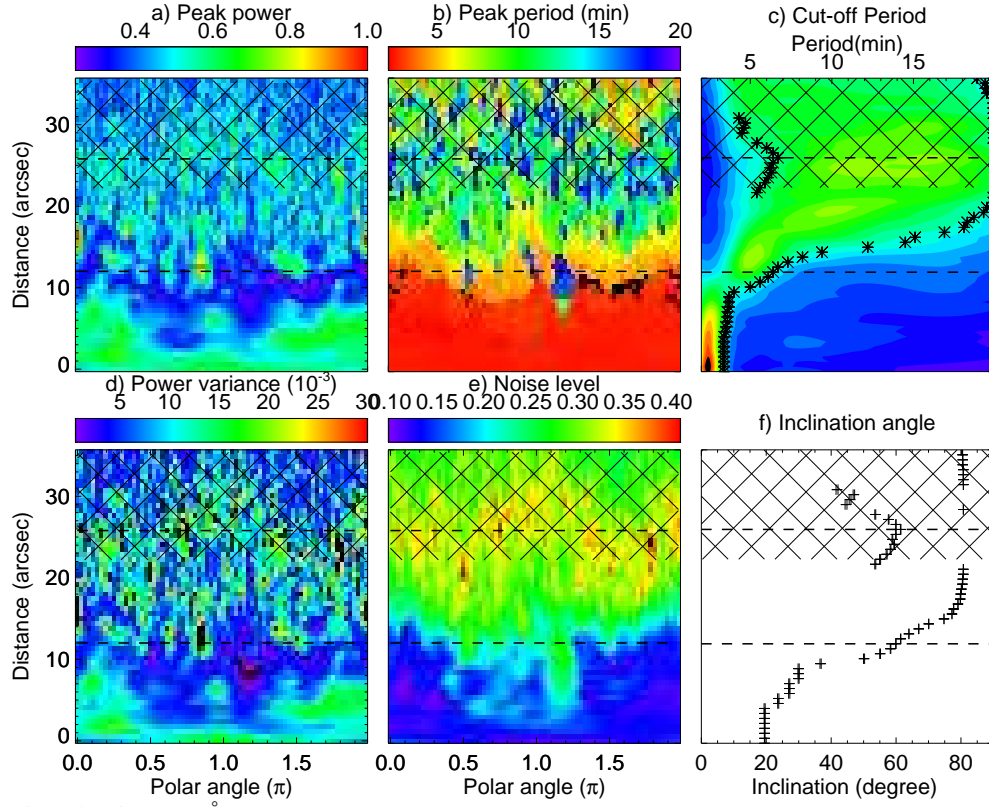


Fig. 4. The same as Fig. 3 but in 1600 Å

2010). The MPFITEXY routine depends on the MPFIT package⁴ (Markwardt 2009). All the three lines are very close to one another, the slopes are 0.80 ± 0.01 ⁵, 0.75 ± 0.01 and 0.74 ± 0.01 for the 1700 Å, 1600 Å and 304 Å data, respectively. The results agree with the empirical relation ($\nu_{\text{peak}} \simeq 1.25\nu_{\text{ac}}$) between the peak and cut-off frequency as suggested in Bogdan & Judge (2006); Tziotziou et al. (2006), but we obtained non-zero intercepts in the linear fits, $-(0.78 \pm 0.01)$ mHz, $-(0.47 \pm 0.01)$ mHz and $-(0.78 \pm 0.01)$ mHz for 1700 Å, 1600 Å and 304 Å, respectively (see Fig. 10). Large deviations from the linear model occur at $\nu_{\text{peak}} \simeq 3$ mHz (5-min band), strongest in 1700 Å data, and also visible in 1600 Å and 304 Å as well.

4.3. Reconstruction of the magnetic field inclination

As described in Sec. 3.2, the results of 1D reconstruction are illustrated in Fig. 3 (304 Å), Fig. 4 (1600 Å) and Fig. 5 (1700 Å). Comparison of our results obtained with the seismological technique with the potential field extrapolation is shown in Fig. 11. The inclination angles were retrieved at 500 km (1700 Å), 1100 km (1600 Å) and 2200 km (304 Å) above the solar surface. The magnetic inclination was estimated with both the theoretical acoustic cut-off frequency $\nu_0 = 5.2$ mHz and the corresponding observationally determined cut-off frequency ν_0^l , where the index l corresponds to the observational channel used in its determination.

Fig. 11 shows clearly that the general profiles of field inclinations reconstructed with the MAG cut-off at 1600 Å, 1700 Å and 304 Å, agree very well with the potential field extrapolation in the region from $0.2r_p$ to $0.8r_p$, where r_p is the average radius

of the penumbra. The average offsets are 32.7/28.8, 27.9/26.6, 30.9/29.7 for ν_0/ν_0^l reconstructions in 1700 Å, 1600 Å and 304 Å, respectively. The results are slightly improved by using the observed maximum cut-off frequency, but the large offsets cannot be fully removed. This implies that the inclined magnetic field is not the only factor that influence the MAG cut-off frequency, it only accounts for 60-80% of the lowering in the cut-off frequency. In the inner umbra (from 0 to $0.2r_p$), the deviations from the potential field extrapolation are about $20^\circ - 30^\circ$. These deviations may arise from using a constant ν_0 ; choosing the observed ν_0^l for the corresponding bandpass appears more realistic. We obtained a flat distribution in all bandpasses in the inner umbra. It implies that the wave characteristics inside the inner umbra may be different from other regions of the sunspot, or that the impact of the plasma temperature needs to be considered as well. We notice that at $0.8r_p - 1.2r_p$ in the 1600 Å and 1700 Å data, a region of low inclination was obtained. In our method, $\cos(\pm\phi) = |\cos(180^\circ \pm \phi)|$ can not be differentiated (the 180° ambiguity problem, see Metcalf et al. 2006). By considering this effect, this low-inclination region in the penumbra border can be connected with the return-flux region with the magnetic vector pointing downwards, instead of upwards. The green asterisk denotes the return flux in the potential magnetic field corrected into $[0^\circ, 90^\circ]$. The results are consistent with the values estimated with the use of the MAG cut-off, both in the inclination and the distance to the sunspot centre. Such behaviour is consistent with the return-flux sunspot model (Fla et al. 1982; Osherovich 1982). The return-flux region is found to spread at about $0.8r_p - 1.2r_p$. If we assume a parabolic shape of the magnetic field lines, the returning flux at about $0.4r_p - 0.6r_p$ extends to the height of about $0.14r_p - 0.26r_p$ and returns to the surface about $0.4 - 0.6r_p$ apart from the source. This effect is less pronounced in the 304 Å data, in which the magnetic field shows a

⁴ <http://cow.physics.wisc.edu/~craigm/idl/idl.html>

⁵ The fit errors less than 0.01 were considered as 0.01.

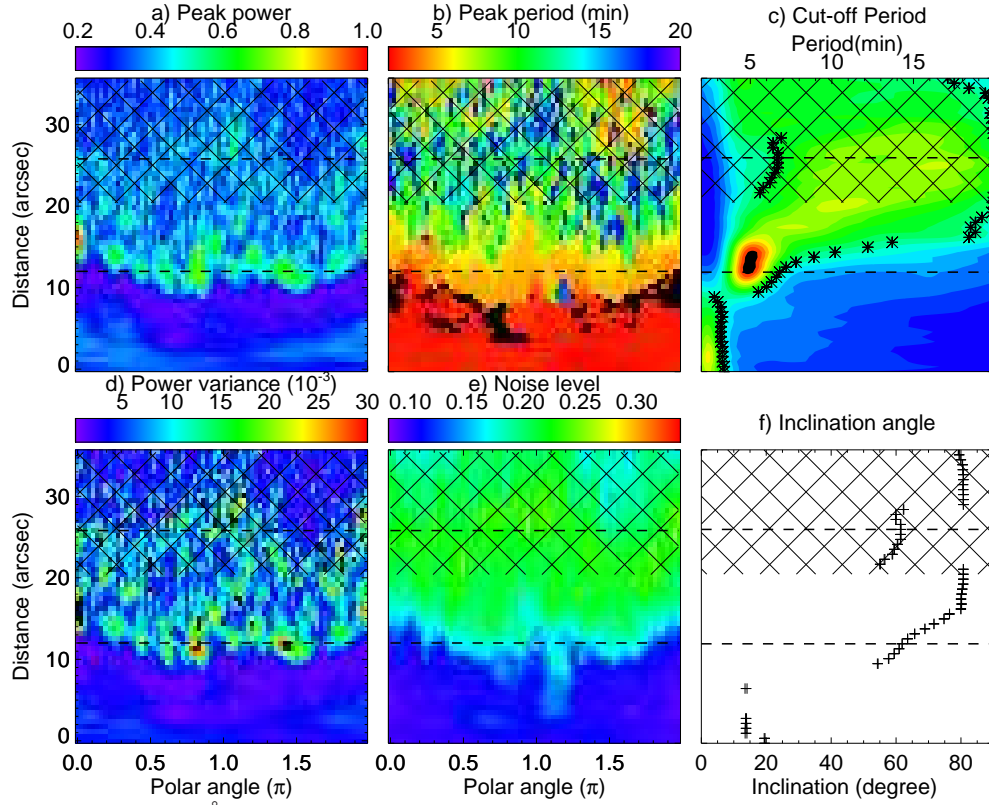


Fig. 5. The same as Fig. 3 but in 1700 Å

steady extension outwards the sunspot. The agreement between the inferred magnetic inclination and the values obtained with the potential field extrapolation is better in the return-flux region compared with the inner sunspot region. The return fluxes were normally found at the periphery of the sunspot penumbra with a weaker magnetic field and higher temperature, so we infer that other effects, e.g. radiative cooling, should be accounted as well to understand the lowering of the MAG cut-off frequency.

In 2D reconstruction, we compare the reconstructed magnetic field inclination, panel (e) of Fig. 6, Fig. 7 and Fig. 8, with the potential field extrapolation shown in Fig. 12. Our method reconstructed the magnetic inclination distribution: both the global profiles, fine structure inside the sunspot umbra and the protrusion at the penumbra. In the 1600 Å and 1700 Å data, the return flux is reconstructed very well. It appears that in 2D geometry, no apparent physics modified the result, except the morphology. The potential field extrapolation reflects the general profiles, including the protrusion structure and the return flux. The average offsets are larger, 41.0, 37.8 and 37.0, which may arise from the error accumulation, since the outliers can not be effectively excluded.

5. Conclusions

We observed the 3D period variations of compressive oscillations in two sunspots. Our results confirm the previous findings that short-period (high-frequency) oscillations are constrained inside the sunspot umbra, while long-period (low-frequency) oscillations are mainly present outside the umbra. Longer the period is, further away the oscillations are observed from the sunspot centre. The predominant oscillation inside the umbra is the well-known 3-min oscillation. The variation over different heights indicates that the 3-min oscillation is not sourced from

the solar interior, rather it is more consistent with the acoustic resonator model (Zhugzhda 2008; Botha et al. 2011). The 5-min oscillations form a ring-shape at the umbra border. We may speculate that the strong power of 5-min oscillations may indicate strong interaction of acoustic waves with the magnetic field, where the local condition favoured the absorption of global solar p -modes (Cally et al. 2003; Schunker & Cally 2006).

We seismologically reconstructed the magnetic field inclination with the use of the Bel & Leroy (1977) formalism, and found its results to be consistent with the results obtained with potential field extrapolation. It confirmed the conclusion in Bel & Leroy (1977) that the inclined magnetic field lowers the cut-off frequency. The MAG-reconstructed magnetic inclinations are generally larger than the potential field extrapolation. The small discrepancy may be attributed to the other effects, e.g. radiative cooling (Centeno et al. 2006, 2009; Felipe et al. 2010). The effect of the magnetic field inclination accounts for about 60-80% of the lowering in the cut-off frequency. The seismological method applied in our study provides an alternative way to reconstruct the magnetic field. Moreover, it may provide the boundary or initial conditions for the magnetic field extrapolation.

In our method, we assumed $\beta \ll 1$, which may be incorrect in some parts of the sunspots. The method can be improved by considering an observational or empirical β profiles at various heights of the sunspots. If the 3D magnetic field vector field is available, the magnetic field strength and inclination can be calculated, we are able to reconstruct the sound speed and local temperature profiles in both 1D and 2D at various heights.

Acknowledgements. DY is supported by MPAGS studentship. MAGPACK2 package for computing solar magnetic fields was developed by T. Sakurai. The work was supported by the RFBR grant N12-02-91161-GFEN-a, 10-02-00153-a, Marie Curie International Research Staff Exchange Scheme Fellowship PIRSES-GA-2011-295272 and the Ministry of Education and Science of the Russian

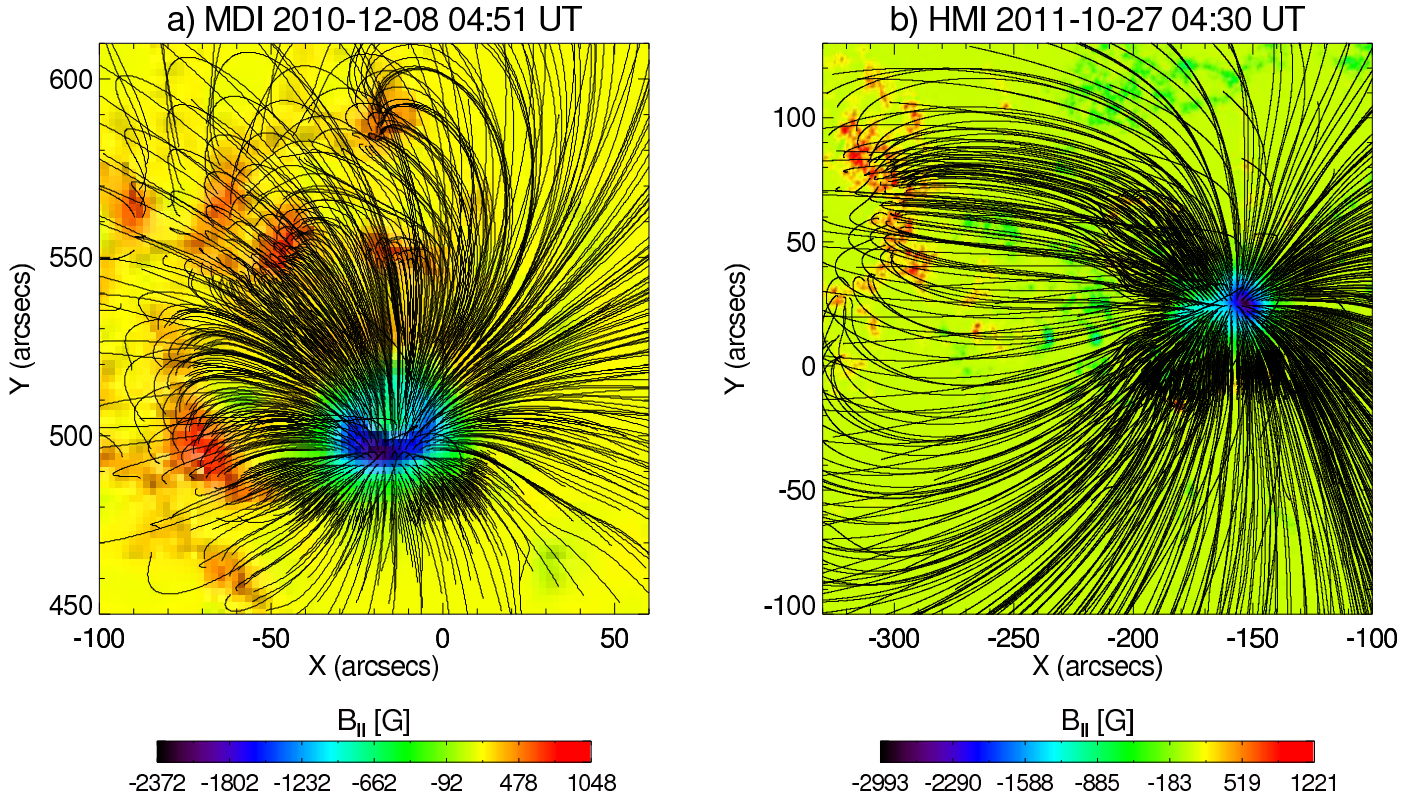


Fig. 9. Results of the potential field extrapolation using the MDI magnetogram for sunspot AR11131 on 08 Dec 2010 (a) and with the HMI magnetogram for sunspot AR11330 on 27 Oct 2011 (b).

- 1 Federation. The AIA data were used as courtesy of the SDO AIA science team.
- 2 This research has made use of NASA's Astrophysics Data System.

3 References

- 4 Bel, N. & Leroy, B. 1977, *A&A*, 55, 239
- 5 Bloomfield, D. S., Lagg, A., & Solanki, S. K. 2007, *ApJ*, 671, 1005
- 6 Boerner, P., Edwards, C., Lemen, J., et al. 2011, *Sol. Phys.*, 316
- 7 Bogdan, T. J. & Judge, P. G. 2006, *Royal Society of London Philosophical Transactions Series A*, 364, 313
- 8 Botha, G. J. J., Arber, T. D., Nakariakov, V. M., & Zhugzhda, Y. D. 2011, *ApJ*, 728, 84
- 9 Cally, P. S., Crouch, A. D., & Braun, D. C. 2003, *MNRAS*, 346, 381
- 10 Centeno, R., Collados, M., & Trujillo Bueno, J. 2006, *ApJ*, 640, 1153
- 11 Centeno, R., Collados, M., & Trujillo Bueno, J. 2009, *ApJ*, 692, 1211
- 12 De Moortel, I., Ireland, J., Hood, A. W., & Walsh, R. W. 2002, *A&A*, 387, L13
- 13 De Pontieu, B., Erdélyi, R., & De Moortel, I. 2005, *ApJ*, 624, L61
- 14 De Pontieu, B., Erdélyi, R., & James, S. P. 2004, *Nature*, 430, 536
- 15 de Wijn, A. G., McIntosh, S. W., & De Pontieu, B. 2009, *ApJ*, 702, L168
- 16 Felipe, T., Khomenko, E., Collados, M., & Beck, C. 2010, *ApJ*, 722, 131
- 17 Fla, T., Skumanich, A., & Osherovich, V. A. 1982, *ApJ*, 261, 700
- 18 Fontenla, J. M., Avrett, E. H., & Loeser, R. 1993, *ApJ*, 406, 319
- 19 Jefferies, S. M., McIntosh, S. W., Armstrong, J. D., et al. 2006, *ApJ*, 648, L151
- 20 Jess, D. B., De Moortel, I., Mathioudakis, M., et al. 2012, *ApJ*, 757, 160
- 21 Lemen, J. R., Title, A. M., Akin, D. J., et al. 2011, *Sol. Phys.*, 172
- 22 Loughhead, R. E. & Bray, R. J. 1958, *Australian Journal of Physics*, 11, 177
- 23 Markwardt, C. B. 2009, in *Astronomical Society of the Pacific Conference Series*, Vol. 411, *Astronomical Data Analysis Software and Systems XVIII*, ed. D. A. Bohlender, D. Durand, & P. Dowler, 251
- 24 Marsh, M. S., Walsh, R. W., & Plunkett, S. 2009, *ApJ*, 697, 1674
- 25 McIntosh, S. W. & Jefferies, S. M. 2006, *ApJ*, 647, L77
- 26 Metcalf, T. R., Leka, K. D., Barnes, G., et al. 2006, *Sol. Phys.*, 237, 267
- 27 Osherovich, V. A. 1982, *Sol. Phys.*, 77, 63
- 28 Reznikova, V. E. & Shibasaki, K. 2012, *ApJ*, 756, 35
- 29 Reznikova, V. E., Shibasaki, K., Sych, R. A., & Nakariakov, V. M. 2012, *ApJ*, 746, 119
- 30 Sakurai, T. 1982, *Sol. Phys.*, 76, 301
- 31 Schunker, H. & Cally, P. S. 2006, *MNRAS*, 372, 551
- 32 Suematsu, Y., Shibata, K., Neshikawa, T., & Kitai, R. 1982, *Sol. Phys.*, 75, 99
- 33 Sych, R., Zaqarashvili, T. V., Nakariakov, V. M., et al. 2012, *A&A*, 539, A23
- 34 Sych, R. A. & Nakariakov, V. M. 2008, *Sol. Phys.*, 248, 395
- 35 Tziotziou, K., Tsiropoulou, G., Mein, N., & Mein, P. 2006, *A&A*, 456, 689
- 36 Wang, T. J., Ofman, L., Davila, J. M., & Mariska, J. T. 2009, *A&A*, 503, L25
- 37 Williams, M. J., Bureau, M., & Cappellari, M. 2010, *MNRAS*, 409, 1330
- 38 Yuan, D. & Nakariakov, V. M. 2012, *A&A*, 543, A9
- 39 Yuan, D., Nakariakov, V. M., Chorley, N., & Foullon, C. 2011, *A&A*, 533, A116
- 40 Zhugzhda, I. D. & Dzhalilov, N. S. 1984, *A&A*, 132, 45
- 41 Zhugzhda, Y. D. 2008, *Sol. Phys.*, 251, 501

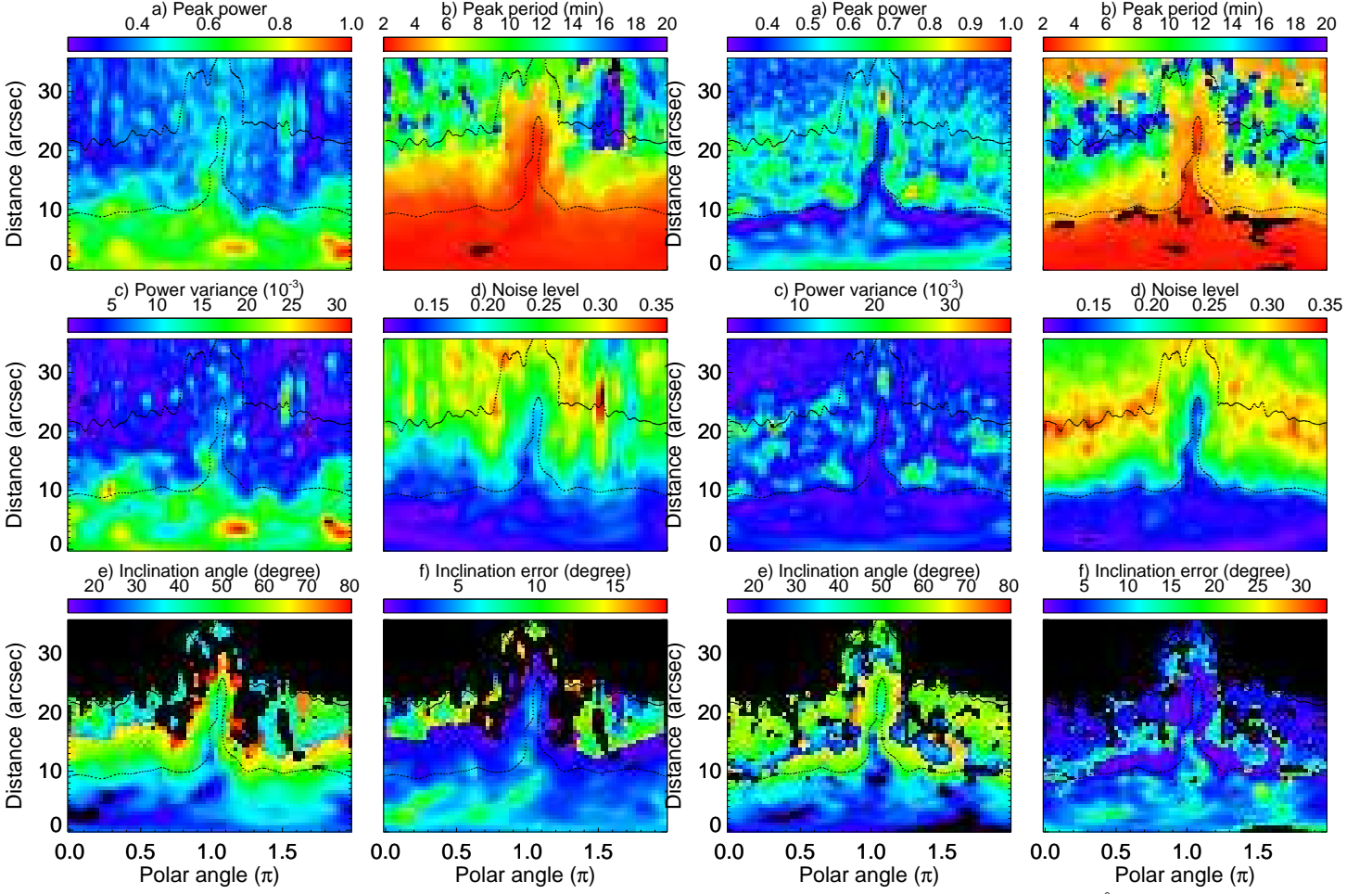


Fig. 6. a) - d) are the same as a), b), d) and e) in Fig. 3. e) and f) are the inclination angle and its uncertainty reconstructed in 2D.

Fig. 7. The same as in Fig. 6 but in 1600 Å

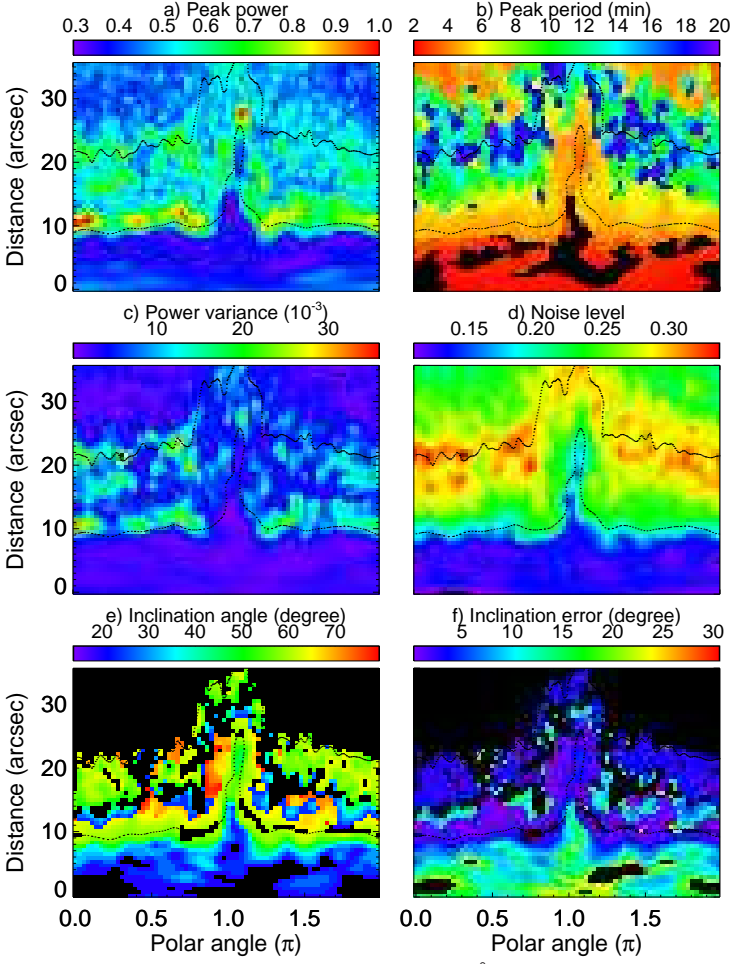


Fig. 8. The same as in Fig. 6 but in 1700 Å

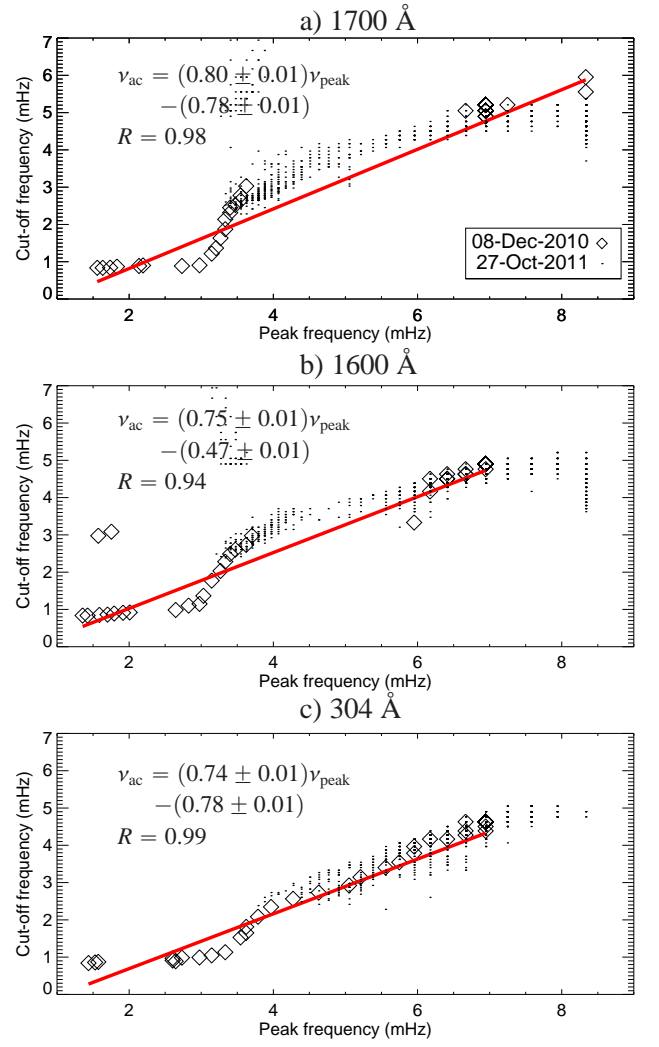


Fig. 10. Correlation between the cut-off frequency and peak frequency for 1700 Å (a), 1600 Å (b) and 304 Å (c) data. The diamond symbols represent the measurement at sunspot AR11131 observed on 08 Dec 2010, while dot symbols indicate the data of sunspot AR11330 observed on 27 Oct 2011. The data are fitted with a linear relationship $\nu_{ac} = a\nu_{peak} + b$, as plotted in red solid line. The fit parameters, as well as the Pearson's correlation coefficient, are displayed in each panel.

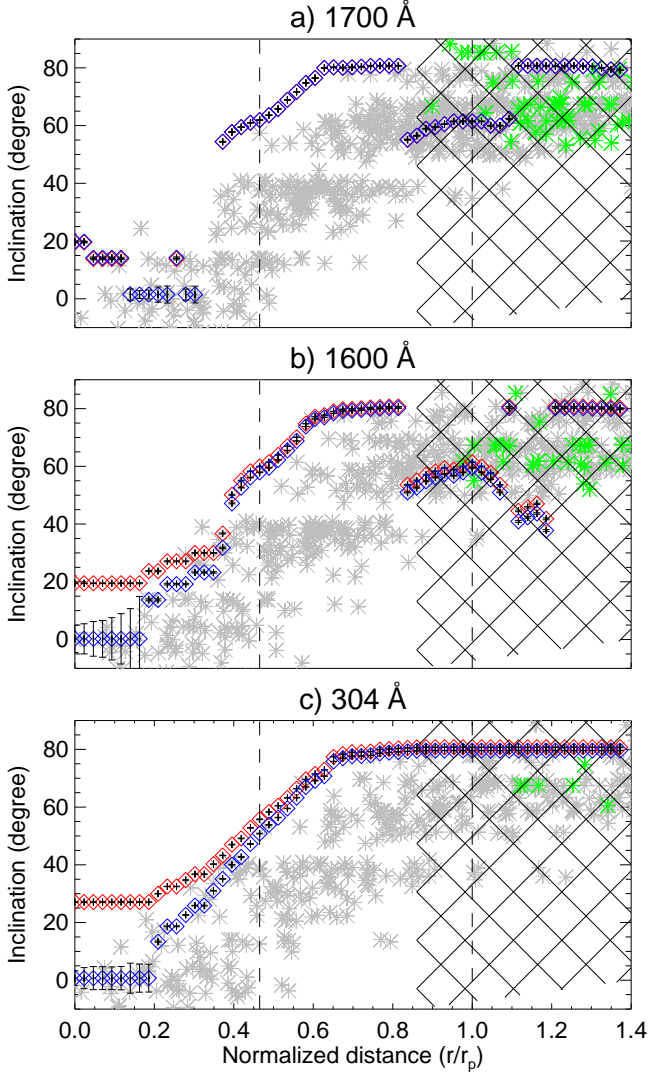


Fig. 11. Comparison of magnetic field inclination reconstructed by magneto-acoustic cut-off with potential field extrapolation for sunspot AR11131 (08 Dec 2010) in 1700 Å (a), 1600 Å (b) and 304 Å (c) bandpasses. The inclination angles obtained with the potential field extrapolation are represented in grey asterisk as the scatter plot, while the data in green asterisks denote the absolute values of inclinations of the return flux. The inclination angles reconstructed with $\nu_0 = 5.2$ mHz are plotted in the red diamonds, while those reconstructed with the observational maximum cut-off frequency ν_0^λ are plotted in blue diamonds. The dashed lines show the border of the sunspot umbra and penumbra, The cross-hatched region marks the measurements below the significant level.

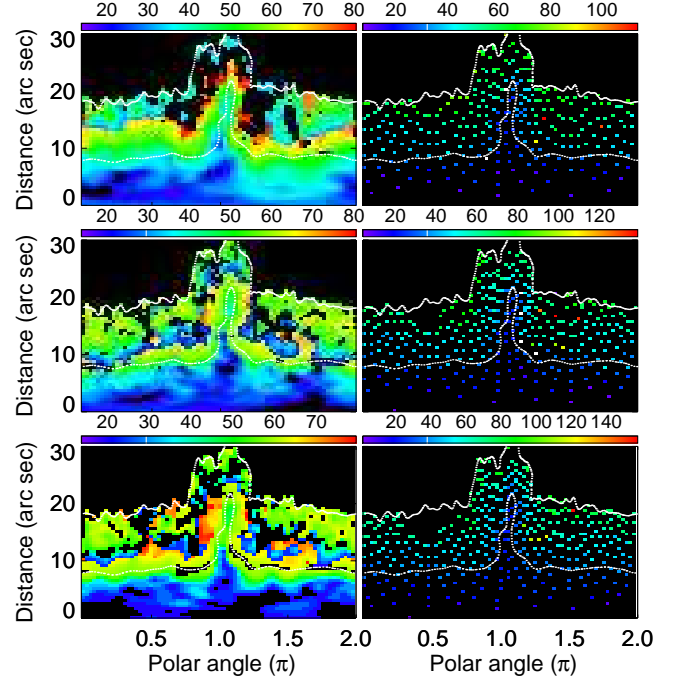


Fig. 12. Left column: magnetic field inclination obtained with ν_0 reconstruction. Right column: the inclination angle obtained from potential field extrapolation for AR11330 on 27 Oct 2011. From top to bottom rows, the panels correspond to 304 Å, 1600 Å and 1700 Å data. The dotted lines mark the umbra and penumbra borders.